Research Square

Preprints are preliminary reports that have not undergone peer review.
They should not be considered conclusive, used to inform clinical practice,
or referenced by the media as validated information.

A robust methodology for the detection of turbulent/non-turbulent interfaces in temporally evolving turbulent flows

Neelakash Biswas

n.biswas20@imperial.ac.uk

Imperial College London

Jiangang Chen

Imperial College London

Oliver R. H. Buxton

Imperial College London

Research Article

Keywords: Turbulent/Non-turbulent interfaces, wakes, entrainment

Posted Date: November 6th, 2026

DOI: https://doi.org/10.21203/rs.3.rs-11459188/v1

License: This work is licensed under a Creative Commons Attribution 4.0 International License.
Read Full License

Additional Declarations: No competing interests reported.

A robust methodology for the detection of turbulent/non-turbulent interfaces in temporally evolving turbulent flows

Neelakash Biswas[1*], Jiangang Chen[1, 2] and Oliver R. H. Buxton[1]

[1*]Department of Aeronautics, Imperial College London, London, SW7 2AZ, UK.

[2]Institute of extreme mechanics, School of Aeronautics, Northwestern Polytechnical University, Xi'an, 710072, China.

*Corresponding author(s). E-mail(s): n.biswas20@imperial.ac.uk;
Contributing authors: jiangang.chen@nwpu.edu.cn;
o.buxton@imperial.ac.uk;

Abstract

A new interface detection technique is proposed to identify turbulent/non-turbulent interfaces (TNTIs) in temporally-evolving flows, and its efficiency in comparison to existing techniques is assessed for two fundamentally different test cases. The first consisted of a temporally-evolving cylinder wake, and the second a decaying stream of grid-turbulence. The turbulent flows were marked with a high Schmidt number dye and combined PIV/PLIF experiments were performed. The TNTIs were identified using PLIF image intensity and intensity-gradient based methods. Since the bulk concentration decayed with time, a time dependent normalisation of the images had to be performed in all methods. A novel intensity-based method was proposed where the intensity field was transformed using a combination of pixel-based intensity and the corresponding cross-stream, $\boldsymbol{y}$, location. The efficacy of the different methods were compared using metrics such as total enstrophy contained within the interface and enstrophy gradient along the interface. The new intensity-based method showed a superior performance as it captured both high total enstrophy and enstrophy gradient.

Keywords: Turbulent/Non-turbulent interfaces, wakes, entrainment

1 Introduction

In many turbulent flows such as jets, wakes, boundary layers and mixing layers, a thin interface demarcates the flow's turbulent core from an outer non-turbulent background flow. This highly convoluted interface is termed as the turbulent/non-turbulent interface (TNTI) (Corrsin and Kistler 1955; Da Silva et al. 2014). The TNTI plays a pivotal role in the evolution of the bounded turbulent region of the flow by influencing the entrainment of mass, momentum, energy and other scalars from the background, into the turbulent core (Townsend 1956; Buxton and Chen 2023; Huang et al. 2023). An accurate detection of the interface is therefore necessary to study the entrainment physics.

Several methods have been adopted to detect TNTIs. Some studies used a small, non-zero threshold value of vorticity magnitude ($|\omega|$) or enstrophy ($\omega_i\omega_i$) to detect the interface (Bisset et al. 2002; Da Silva et al. 2014). Here, vorticity, ω_i is the curl of velocity u_i, defined as $\omega_i = \epsilon_{ijk}\frac{\partial u_j}{\partial x_k}$ (ϵ_{ijk} denotes the Levi-Civita symbol). Other studies used a passive scalar to mark this edge of turbulence. For instance, Antonia (1981) used temperature as an indicator of turbulence by slightly raising the temperature of the turbulent fluid. This method however had limitations due to high thermal diffusivity in gas flows (low Prandtl number, $Pr \sim 1$). Planar laser induced fluorescence (PLIF) based studies using a high Schmidt number ($Sc \sim 2000$) dye in water has been a more attractive option in experimental characterization of TNTIs (Prasad and Sreenivasan 1989; Westerweel et al. 2005; Mistry et al. 2016; Kankanwadi and Buxton 2020; Kohan and Gaskin 2022).

Prasad and Sreenivasan (1989) first proposed a method to objectively identify TNTIs in a turbulent jet using PLIF image intensity (which we denote I). They tested a range of intensity thresholds (denoted by I_{th}) and conditionally averaged the image based on the threshold as follows:

$$\langle I \rangle = \frac{\sum(I|I > I_{th})}{N(I > I_{th})} \tag{1}$$

i.e. for a given I_{th}, $\langle I \rangle$ was obtained by averaging the intensity over all the pixels for which $I > I_{th}$. Here N refers to the number of pixels in the image that satisfy this condition. The correct threshold was then selected by looking at how $\langle I \rangle$ varied with I_{th}. The chosen threshold corresponded to the point where the second derivative of the $\langle I \rangle$, I_{th} curve crossed zero. This method was followed in several later works (Westerweel et al. 2005; Mistry et al. 2016; Kankanwadi and Buxton 2020; Kohan and Gaskin 2022). When considering a series of images, the averaging was done over all images, yielding a single $\langle I \rangle$, I_{th} curve and hence a single I_{th}. In experiments where the image intensity varied significantly in space, e.g. due to mixing of non-dyed background fluid into the primary flow, a spatial normalisation was necessary. For instance, in a cylinder wake, the time-averaged centreline intensity was used to normalise the images before finding an appropriate threshold (Chen and Buxton 2023).

Some works considered the gradient of the light intensity instead of intensity itself (Kankanwadi and Buxton 2020; Kohan and Gaskin 2022; Chen and Buxton 2024). Chen and Buxton (2024) found the threshold in a similar way by performing a conditional averaging over the intensity gradient ($\langle \nabla I \rangle$). On the other hand, Kankanwadi

and Buxton (2020) adopted a more complex approach by calculating the mean esntrophy out of the wake (based on concurrently obtained PIV-derived velocity fields, alongside the PLIF) as a function of light intensity gradient thresholds. Highlighting the limitations of light intensity based methods, they argued that such methods could be insufficient due to possible variability in the dye injection rate or the laser power output with time. Furthermore, intensity based results could be contaminated due to the 'halo' effect caused by secondary fluorescence of the dye in and around high concentration blobs (Baj et al. 2016). Nonetheless, gradient based methods also offer unique challenges. Firstly, computing the gradient itself can introduce noise. Secondly, encountering the chosen gradient-based threshold within the turbulent core is more likely in comparison to an equivalent threshold based on intensity itself. This could increase the chances of false detection or detection of internal contours (Prasad and Sreenivasan 1989). A detailed study comparing the efficacy of intensity and intensity gradient based methods has not been performed.

In numerical simulations, simulating high Sc passive scalars typically used in experiments is not feasible. TNTIs obtained using a low Sc scalar (typically $Sc = 1$ is used in numerical simulations such that the advection diffusion equations can be solved on the same grid) have been shown to be significantly different from those obtained using vorticity (Silva and da Silva 2017). Therefore, TNTIs have generally been identified using a threshold based on vorticity magnitude or enstrophy (Bisset et al. 2002; Taveira et al. 2013; Da Silva et al. 2014; Watanabe et al. 2015, 2017). The process of identifying the threshold has been similar to that reported above, the only difference being a conditional averaging based on vorticity magnitude or enstrophy is generally not performed. Instead, for a given vorticity/enstrophy-based threshold, the fraction of the volume of the turbulent region (with vorticity/enstrophy larger than the threshold) is quantified as a function of the threshold. We denote this turbulent volume fraction as f. A threshold is chosen from the region where f changes slowly with increasing threshold or shows a plateau region (Da Silva et al. 2014; Silva and da Silva 2017; Taveira et al. 2013; Watanabe et al. 2015, 2017). Note that the same process can also be followed using PLIF image intensity.

The bulk of previous PLIF-based experimental studies on TNTIs have considered flows that are spatially evolving (Prasad and Sreenivasan 1989; Westerweel et al. 2005; Mistry et al. 2016; Kankanwadi and Buxton 2020). Here, f can be expected to remain relatively constant over time. However, when the flow is temporally evolving, f increases significantly with time. As a result, the quantity may not show a clear plateau with the threshold, making it significantly more challenging to identify a single threshold that identifies the correct TNTI at all times. Such time evolving flows are instrumental in studying the interface dynamics from a Lagrangian perspective (Taveira et al. 2013), yet experimental works on such flows are scarce. Consequently, a robust methodology for identifying the TNTI in such flows is also missing.

In this work, we report the results from two separate experimental campaigns. The first campaign considered a temporally-evolving cylinder wake, and the second campaign considered a decaying stream of grid turbulence (evolving in time). We propose a novel method for identifying TNTIs in such flows, indeed to the authors'

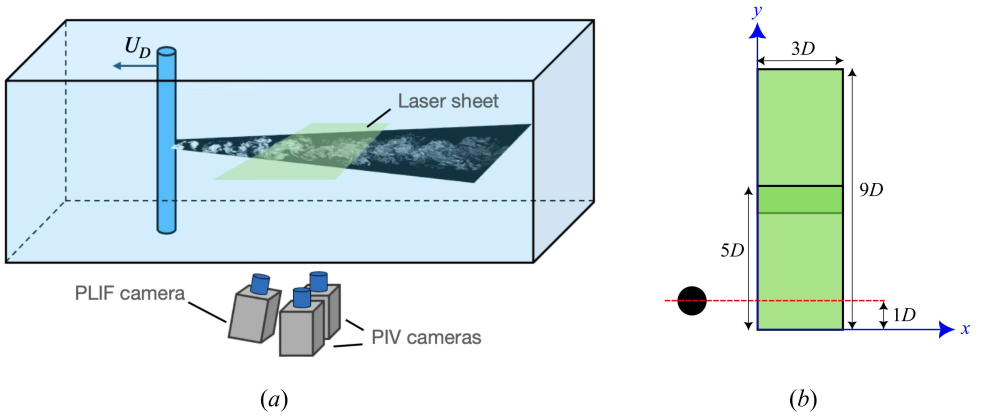


Fig. 1 Schematic of the experimental setup capturing the cylinder wake. (a) shows the positioning of the cameras used for simultaneous PIV and PLIF measurements. (b) shows the stitched PIV FOV that matched with the PLIF FOV. The black circle shows the position of the cylinder with respect to the FOV and the red dashed line shows the path along which the cylinder moves to the left (along $-x$).

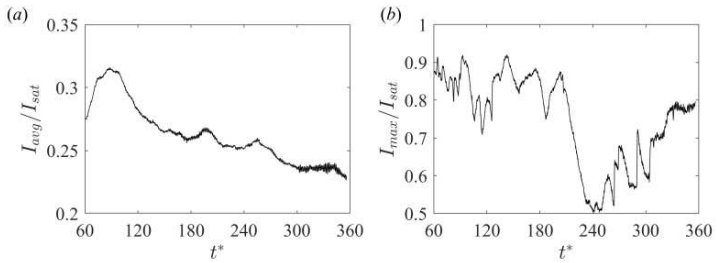


Fig. 2 Time history of (a) average and (b) maximum image intensity in the cylinder wake. t^* denotes the normalised time ($t^* = tU_D/D$) measured from the time the cylinder leaves the left edge of the FOV.

knowledge this is the first such method proposed in the literature, and compare its efficacy with existing methods, developed for spatially-evolving flows.

2 Temporally-evolving wake of a cylinder

The experiments were carried out in the hydrodynamics flume in the Department of Aeronautics at Imperial College London. In the first experimental campaign, combined planar PIV and PLIF experiments were carried out to capture the wake of a moving cylinder. The experimental setup is shown in figure 1(a) and was the same as that discussed in (Chen and Buxton 2026). The cylinder had a diameter $D = 1$ cm and was dragged upstream at a constant velocity ($U_D = 0.3$m/s). Two PIV cameras and a PLIF camera were placed underneath the flume focusing on the same target field of view (FOV), having a streamwise extent of $3D$ and transverse extent of $9D$, at small viewing angles. The cameras were operated in cinematographic mode yielding an acquisition

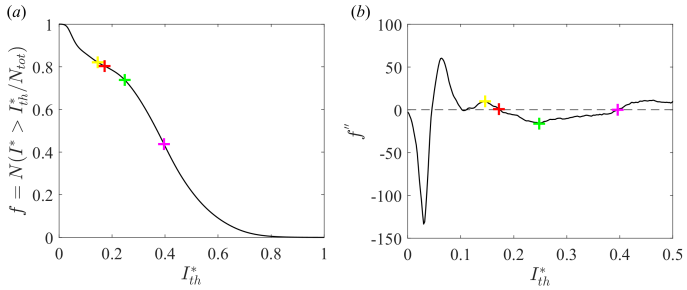


Fig. 3 Variation of (a) image-intensity fraction (f) and (b) its second derivative with intensity threshold I^*_{th}. Here every image is normalised by the maximum intensity (I_{max}) in that image. The points of interest are marked by $+$.

frequency $f_{aq} = 200$Hz. The raw PIV images were processed in PIVlab (Thielicke and Stamhuis 2014). The adaptive cross-correlation algorithm in PIVlab used a multi-pass, fast Fourier transform to determine the average particle displacement. An initial interrogation area (IA) of 96 $\times$ 96 pixels was reduced in three passes, with a final IA size 24 $\times$ 24 pixels with 50 % overlap in the x and y directions. The time (t) was measured from the moment the cylinder crossed and exited the FOV and is non-dimensionalised by D and U_D giving $t^* = tU_D/D$. In this work we ustilised data in the time interval $60.45 \leq t^* \leq 356.1$ which corresponds to 9.86 seconds or 1972 images. This range of t^* was chosen since for lower t^*, the PLIF images were locally saturated. Note that nt^* spatially maps to nD in this case.

Figure 2(a) shows the average image intensity (I_{avg}) with time, which shows a decaying trend in general, whilst the maximum pixel based image intensity (I_{max}) shows a more complex non-monotonic time variation in figure 2(b). Here I_{sat} is the saturation intensity level. Since the average dye concentration (intensity) changes with time, a time-dependent normalization is necessary as we will discuss in the subsequent sections. Throughout the manuscript, a normalized image is denoted by I^*. Once normalization is performed, we seek to objectively identify a single threshold I^*_{th} that identifies the correct interface at all times.

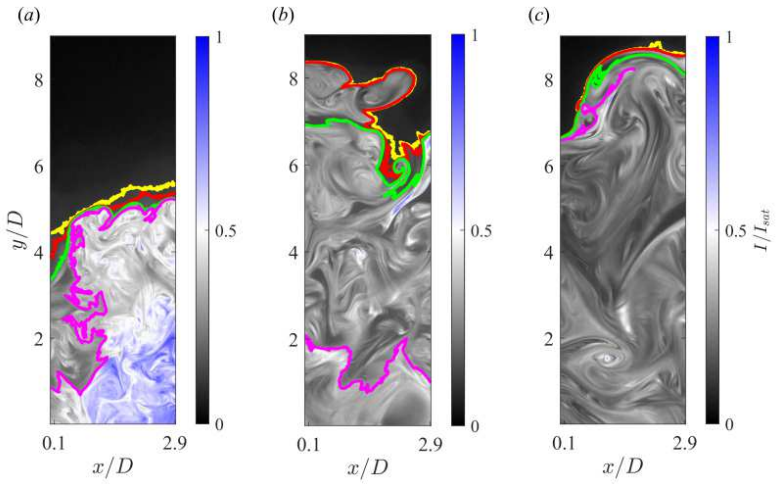


Fig. 4 Interfaces detected at (a) $t^* = 60.45$, (b) $t^* = 208.35$ and (c) $t^* = 356.1$. The differently coloured interfaces correspond to the I^*_{th} values marked with the same colour in figure 3. Every image is normalised by the maximum intensity in that image.

2.1 M1: Normalization using maximum intensity

The easiest way to normalize the PLIF images is with I_{max}. We denote this as method 1 (M1). As discussed in the introduction, after normalization, the fraction of the grid points (denoted by f) with intensity $I^* > I^*_{th}$ over all 1972 images is obtained as a function of I^*_{th}. Note that this process did not require the identification of the interfaces. If there was a high intensity region outside the wake (so-called islands, which may result from a large-scale detrainment event but are typically associated with a two-dimensional representation of the three-dimensional topology of the interface, i.e. tea-cup handles (Kohan and Gaskin 2020)), the grid points in the regions were still counted as long as $I^* > I^*_{th}$. The variation of f is shown in figure 3(a). Here, we do not see a prominent plateau region, making it difficult to visually identify the most suitable I^*_{th}. Therefore we look at the second derivative of f (figure 3(b)). Previously, some studies have used the inflection points ($f'' = 0$) as the threshold (Prasad and Sreenivasan 1989; Mistry et al. 2016). Here however, we see multiple inflection points. The thresholds of interest, including the local extrema and inflection points, are marked in figure 3 with a + symbol. The interfaces corresponding to these thresholds are shown in figure 4 at 3 time instances using the same colours as the symbols. The interfaces are identified as the longest continuous contour at the chosen threshold value.

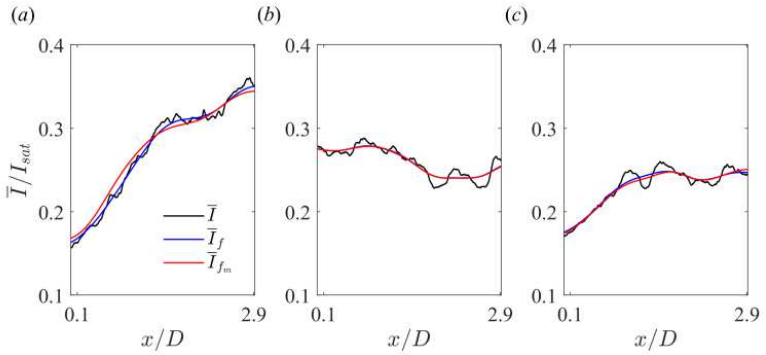


Fig. 5 Normalising average images ($\bar{I}$) at (a) $t^* = 60.45$, (b) $t^* = 208.35$ and (c) $t^* = 356.1$. The images are first filtered ($\bar{I}_f$) and thereafter moving-averaged ($\bar{I}_{f_m}$).

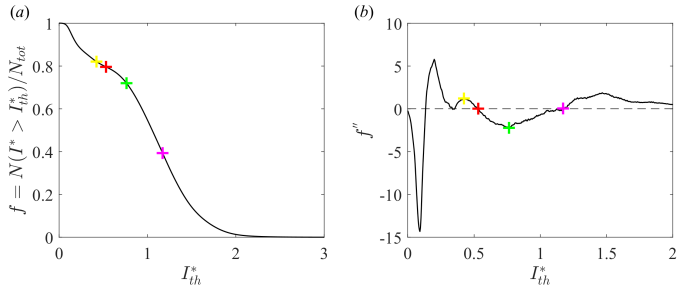


Fig. 6 Variation of (a) image-intensity fraction (f) and (b) its second derivative with concentration threshold I^*_{th}. Here, the images are averaged with spatio-temporally averaged intensity (as shown in figure 5). The points of interest are marked by +.

Note that none of the thresholds yield the correct interface at all times. The thresholds marked by + and + do the best job. However, threshold + is still inaccurate at smaller t^* and threshold + misses a part of the wake for larger t^*. Any of the thresholds lower than + are more gentle (overestimating the extent of turbulence). On the other hand, any of the thresholds beyond + are too aggressive (missing a significant proportion of the wake). A threshold between + and + could yield better results, but such a threshold does not possess a geometrical significance and hence defeats the purpose of the method being objective.

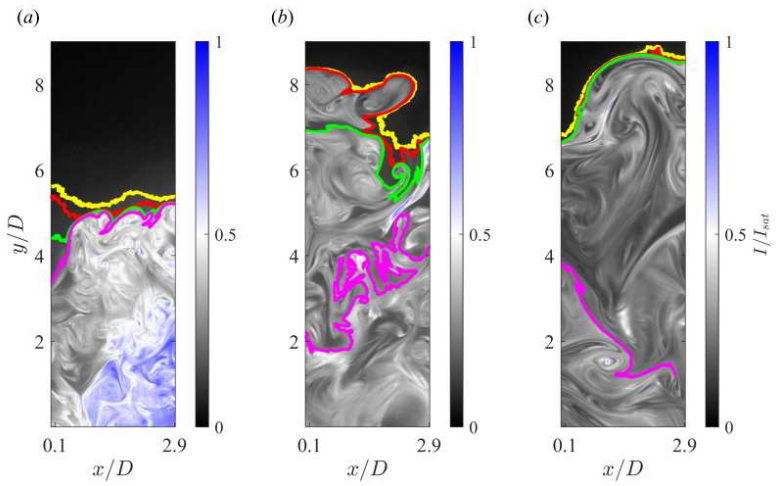


Fig. 7 Interfaces detected at (a) $t^* = 60.45$, (b) $t^* = 208.35$ and (c) $t^* = 356.1$. The differently coloured interfaces correspond to the I^*_{th} values marked with the same colour in figure 6. Every image is normalised by spatio-temporally averaged intensity.

2.2 M2: Normalisation using spatio-temporally averaged intensity

Normalising the images with I_{max} could be inadequate due to the spatial inhomogenity of the intensity field and due to the three dimensional effects. The fact that the time evolution of I_{max} differs significantly from that of I_{avg} (figure 2) testifies to this. Therefore, a normalising intensity more connected to the average spatial and temporal evolution of the intensity field is sought. Here, each image $I(x, y)$ is first averaged along y yielding $\bar{I}(x)$. These one-dimensional images are shown in figure 5 (black lines) at the three selected time instances. Thereafter, a low-pass filtering with cutoff wavelength λ_x was performed. The spatially filtered images are denoted by $\bar{I}_f(x)$ and are shown in blue in figure 5. Finally, a moving-averaging procedure (with window length m_t) was performed over time. The values of λ_x and m_t were carefully chosen. Nevertheless, the following results did not depend significantly on the filtering or averaging process. The spatially filtered and temporally moving-averaged one dimensional images are used to normalise the corresponding original images. This method is termed as method 2 (M2).

The variation of the image-intensity fraction (f) and its second derivative are shown in figure 6 for M2. However, even with this normalisation, f shows multiple inflection points and the general trend of $f^{''}$ looks similar to that obtained for M1. The thresholds of interest are marked in figure 6 and the interfaces obtained using them are shown in figure 7 with the same colours. Similarly to method M1, the thresholds marked with + (inflection point) and + (local minima) do the best job. Other points are either too gentle or too aggressive. Interestingly, a closer observation reveals that the two best cases for M2 work slightly better than the best two cases for M1, especially that + for M2 marks the interface better for the largest t^* compared to + for M1.

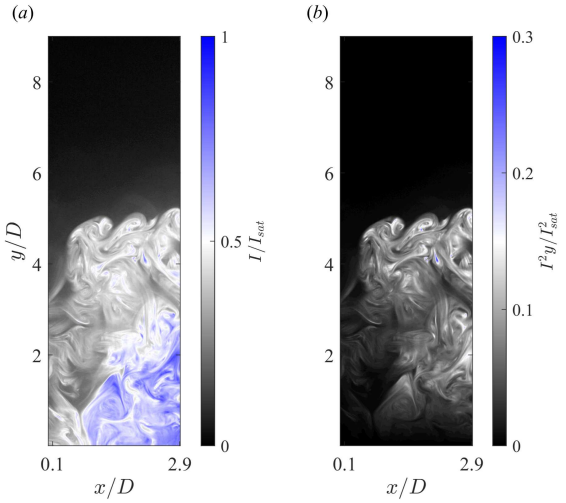


Fig. 8 (a) original image and (b) transformed image at $t^* = 60.45$.

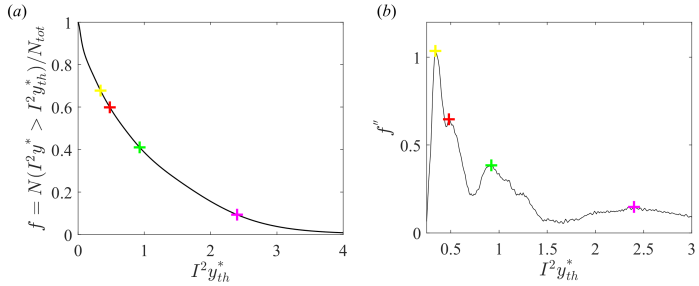


Fig. 9 Variation of (a) image-intensity fraction (f) and (b) its second derivative with threshold $I^2y^*_{th}$. Here, the transformed images are averaged with spatio-temporally averaged transformed intensity. The points of interest are marked by +.

2.3 M3: Normalisation using spatio-temporally averaged transformed intensity

The shape of a TNTI can be convoluted and at places, the interface may tend to fall back in on itself, *i.e.* the interface may exist at multiple y locations for a given x location (Bisset et al. 2002). An example of this can be seen in figure 4(b). In such instances, it is a common practice to only retain the outermost y point of the interface, thus creating an interface envelope (Westerweel et al. 2005; Kankanwadi and Buxton 2020). Analogous to this approach, we consider transforming the images such that the outer most points of the interface in the images are assigned a higher 'transformed intensity'. This transformed intensity could have a form as simple as $I^n y^m$. Here y is taken as an array having values from 0 to 1, 1 at the top edge of the image and zero at the bottom. The dimension of $I^n y^m$ is therefore the same as that of I. n and m can be any integer or fraction and may well be different for different cases. However, $n > m$ ensures that the contribution from the actual image intensity is higher than

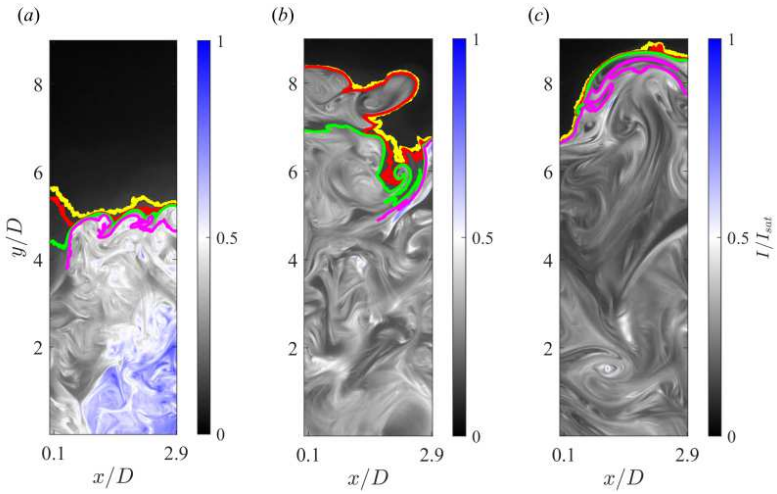


Fig. 10 Interfaces detected at (a) $t^* = 60.45$, (b) $t^* = 208.35$ and (c) $t^* = 356.1$. The differently coloured interfaces correspond to the $I^2 y^*_{th}$ values marked with the same colour in figure 9. Each transformed image is normalised with the spanwise averaged transformed image.

that from y. For the present cases, we tested different values of n keeping m constant and equal to 1 and found $n = 2$ to be the most effective. As an example, the original and transformed images ($I^2 y$) at $t^* = 60.45$ are shown in figure 8. Note that this process attenuates the intensity in the lower part of the image and promotes intensity in the vicinity of the interface we are interested in. Consequently, this approach reduces the likelihood of detecting the chosen threshold value deep inside the wake and hence reduces the chances of detecting a false internal contour.

The transformed images are thereafter averaged in y as before to produce the one dimensional transformed images ($\overline{I^2 y}(x)$). They were next filtered, a moving average was then calculated, and ultimately they were used to normalise the transformed images. This approach is termed as method 3 (M3). The variation of f and f'' with $I^2 y^*_{th}$ for this case is shown in figure 9. Interestingly, for this normalisation, f does not show any inflection points and f'' shows very mild changes in the gradients. Four local maxima are identified. The interfaces corresponding to these thresholds are shown in figure 10. Note that thresholds + and + behave similarly to the best two thresholds found for M1 and M2. In fact the interfaces look very similar to those obtained with M2. However, at $t^* = 60.45$, point + of M3 does a slightly better job than + of M2. Nevertheless, it would be premature to choose a better method simply based on a single snapshot instead of considering the full time series. We will be doing this exercise in section 2.5.

2.4 M4: Intensity gradient based method

As discussed in the introduction, intensity gradient based methods can be useful where experimental artefacts (such as secondary fluorescence (Baj et al. 2016)) is significant. However, the method on it's own can be prone to noise and can be harder to implement numerically as we will be showing.

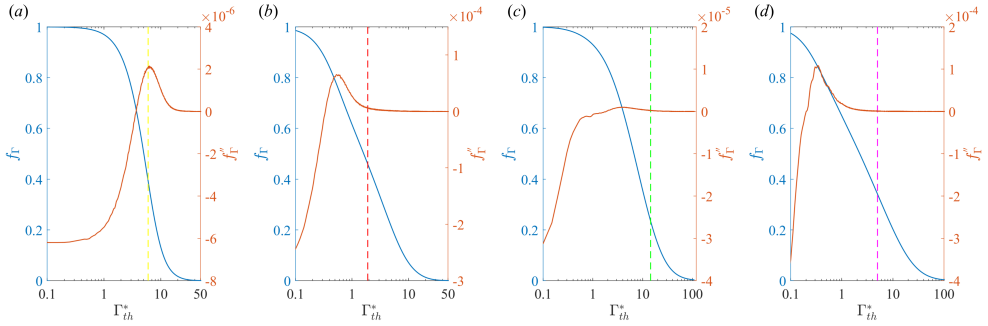


Fig. 11 Variation of intensity gradient fraction (f_Γ) (a) without and (b) with filtering. (c) and (d) show the gradient fraction of the transformed intensity (I^2y) (c) without and (d) with filtering. The dashed vertical line shows the chosen threshold.

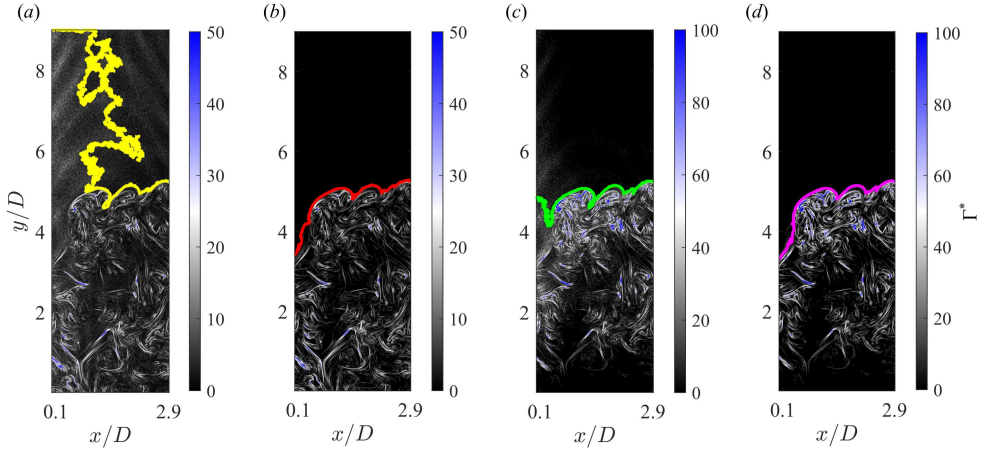


Fig. 12 Normalised intensity gradient field (a) without and (b) with filtering at $t^* = 60.45$. Panels (c) and (d) show the same based on the transformed intensity (I^2y) (c) without and (d) with filtering. The coloured lines show the interfaces detected based on the thresholds marked by the same colours in figure 11.

Before computing the gradient, the images are normalised in the same way as discussed in section 2.2. The magnitude of the normalised intensity gradient is then defined as $\Gamma^* = D|\nabla I^*|$ (where D is the cylinder diameter). The numerical gradient function in MATLAB is used which calculates the central difference at the interior points and one-sided difference at the edges. Thereafter, the fraction of grid points with $\Gamma^* > \Gamma^*_{th}$ is calculated as a function of the threshold Γ^*_{th} as discussed earlier. We denote this intensity gradient based fraction as f_Γ. The variation of f_Γ and its second derivative is shown in figure 11(a). The best working threshold is shown by the vertical dashed line which closely coincides with the local maxima of the second derivative. The interface is then simply identified as the longest continuous contour at the selected threshold value. The intensity gradient field at $t^* = 60.45$ is shown in figure 12(a) and the yellow curve shows the detected interface. Note that, the chosen threshold value

manages to detect only a part of the true interface. The rest of the detected interface erroneously propagates into the non-turbulent background due to the elevated noise level associated with the gradient computation. Similar noisy interfaces were observed throughout the time series which led us to conclude that some degree of filtering of the raw images was necessary before computing the gradient. Here we stress the fact that the intensity based methods did not require any filtering of the raw images.

Prior to computing the gradient, the images were filtered using the Non-Local Means (NLM) filter with a moderate degree of smoothness = 0.01 (Buades et al. 2005). This filter is appropriate for removing noise while preserving sharp edges. Note that we do not intend to compare the effectiveness of other filters in this work and we simply use this filter as an example. The filtered images were then normalised in the same way and the gradients of the normalised images were computed. An example of the gradient field after filtering is shown in figure 12(b) at $t^* = 60.45$. The noise level in the background is drastically reduced while the gradients inside the wake remain largely unaltered. Slight changes to the chosen degree of smoothness did not make a discernible difference to the gradient field. The interface corresponding to the best working threshold is shown in red and it marks the wake edge nicely. f_Γ for this case is shown in figure 11(b). Although the chosen threshold works well, the threshold cannot be determined objectively from $f_\Gamma^{''}$ unlike the intensity based methods.

One could also compute the gradients of the transformed images discussed in section 2.3. The gradient field of the transformed unfiltered image at $t^* = 60.45$ is shown in figure 12(c). Note that the detected interface marks the wake edge much better (than in figure 12(a)), albeit with some noise towards the left edge. This again highlights that the proposed transformation can be used as a simple tool to improve the overall interface detection. The best looking interfaces were obtained when the gradients of the transformed filtered images were considered (figure 12(d)). The variation of f_Γ for these two cases are shown in figure 11(c) and (d) respectively. The best working thresholds still do not correspond to a geometrically meaningful value.

Summarising this section, we can say that the gradient-based methods can be useful but they are inherently noisy. Therefore some level of image pre-processing or filtering might be a necessity which is not the case for intensity-based methods. For gradient-based methods, it is more difficult to objectively identify the best working threshold compared to the intensity based counterpart, at least for the current problem.

2.5 Choosing the best threshold/method

The previous analysis attempted to identify the best working threshold values for the methods M1-M4. However, it is not possible to discern which threshold or method works the best over the entire time series just based on the three time instances. A more robust statistic showcasing the efficacy of a method/threshold is thus sought. For this, we made use of the PIV velocity fields obtained simultaneously to the PLIF. Note that if the chosen threshold is on the aggressive side, the detected interface would miss a significant part of the turbulent core (and associated enstrophy). Similarly, if the threshold is too gentle, the detected interface could be situated well inside the irrotational region. In such a scenario, the detected interface would capture the total enstrophy, but the enstrophy gradient along the interface would be negligible. Note

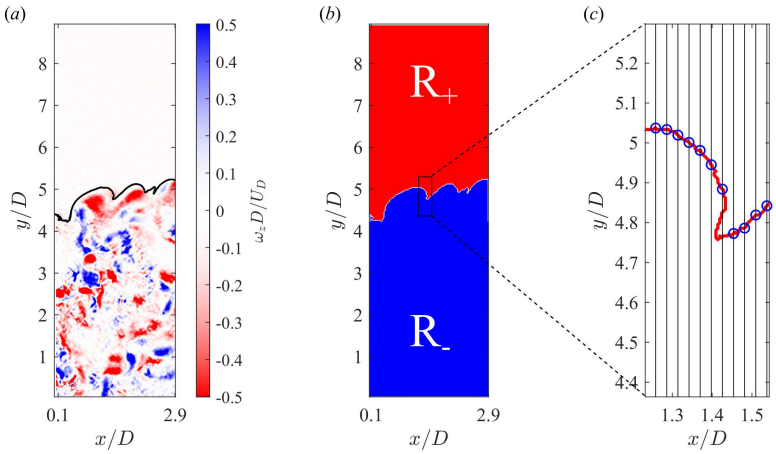


Fig. 13 (a) Vorticity field at $t^* = 60.45$. The interface (in black) is obtained using threshold + of M3. (b) shows how the PIV grid points are separated into two zones, R_-: within the wake, R_+: outside the wake. (c) shows a zoomed part of the interface. The vertical lines are drawn at the x locations of the PIV grid. The farthest intersection points of these lines and the interface are marked by the blue circles. The enstrophy gradient is computed on these points and is averaged along the interface.

that the TNTI is defined as a region in which there is a rapid adjustment of the enstrophy from a zero (or close to zero) level in the background to a non-zero level in the turbulent core over a very short distance, i.e. O(Taylor microscales) yielding a sharp gradient at the irrotational boundary (the outermost surface of the TNTI) (Da Silva et al. 2014). Therefore, we argue that the ideal method/threshold should find a balance between capturing the total enstrophy bounded within the interface, and a large enough enstrophy gradient found at the interface location itself. This process is systematically depicted in figure 13. Figure 13(a) shows the vorticity field at $t^* = 60.45$. The scalar interface obtained using threshold + of M3 is overlayed. The interface captures the wake well. Now, note that the PLIF grid was ≈ 6 times finer than the PIV grid and the points on the two grids did not coincide. Every point on the PIV grid was carefully located with respect to the interface (obtained on the PLIF grid). In figure 13(b), the points within the wake (located in the zone R_-) are marked in blue and those outside (in zone R_+) are marked in red. The total enstrophy in R_- ($\sum_{R_-} \omega_z^2$) is obtained and is divided by the total enstrophy in the whole FOV ($\sum \omega_z^2$). This ratio should ideally be equal to one. However, due to a combination of factors such as measurement noise, presence of non-zero vorticity in the freestream of the experimental facility, inaccuracy of the interface detection method and three dimensional effects (typically yielding the "islands" discussed previously), this ratio is generally < 1 and it vaires with time. Interestingly Kohan and Gaskin (2020) reported that the detached islands constituted 3.81% of the turbulent fluid in a turbulent jet. Following this, we only consider a method/threshold to be effective if it captures at least 96% of the total enstrophy in a time averaged sense.

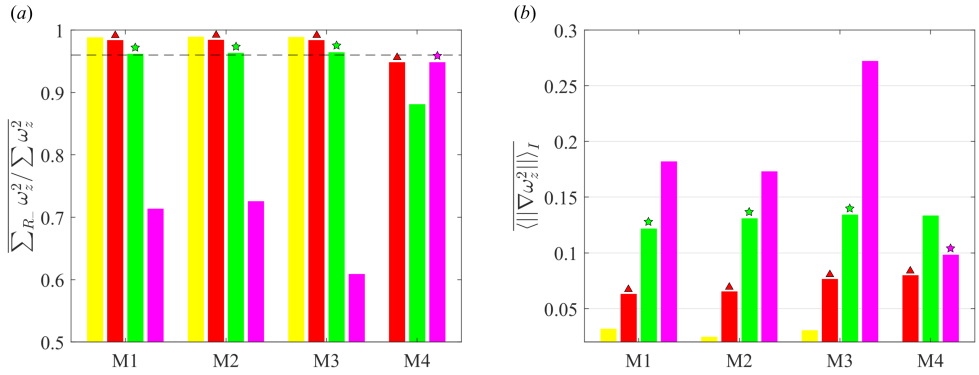


Fig. 14 (a) shows the fraction of the total enstrophy in the FOV captured by the interface (*i.e.* enstrophy contained in zone R_-) averaged in time for the different methods and selected thresholds. A horizontal dashed line is drawn at $\overline{\sum_{R_-} \omega_z^2 / \sum \omega_z^2} = 0.96$. (b) shows the time averaged magnitudes of enstrophy gradient averaged over the interface for the same methods and threshold values. Here M1-M3 are image-intensity based methods and M4 denotes the gradient based method. M3 is the I^2y method. The symbols ▲ and ⋆ denote the two best cases from each method.

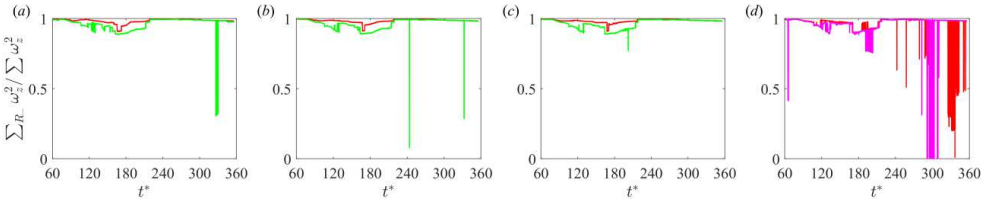


Fig. 15 The fraction of the total enstrophy in the FOV captured by the interface as a function of time for the methods (a) M1, (b) M2, (c) M3 and (d) M4. The different colours correspond to the two selected best cases from each method (marked by the symbols ▲ and ⋆ in figure 14).

Next we look at the enstrophy gradients on the interface and average it over the interface length (denoted as $\langle \|\nabla \omega_z^2\| \rangle_I$). However, care must be taken during this averaging process since different methods can yield different interface lengths for the same image and averaging over different lengths can make comparison difficult. Accordingly, after detecting the y-locations of the interface from the PLIF images, these are sampled at the discrete set of x-locations from the PIV grid. This is shown in figure 13(c). Here the vertical lines are drawn at the x locations of the PIV grid. The y locations corresponding to the farthest point of interaction between the vertical lines and the interface (shown by the blue circles) are used. As a result, for every threshold/method, the enstrophy gradients were averaged over the same interface length. Note that the average enstrophy gradient is not maximum at the irrotational boundary. It reaches its maximum value well inside the TNTI. Therefore, we only use this quantity as a secondary criterion. We look at the average enstrophy gradient, given that more than 96% of the total enstrophy is captured.

The ratio $\sum_{R_-} \omega_z^2 / \sum \omega_z^2$ is obtained as a function of time for all the thresholds/methods and thereafter averaged over time. This is shown in figure 14(a).

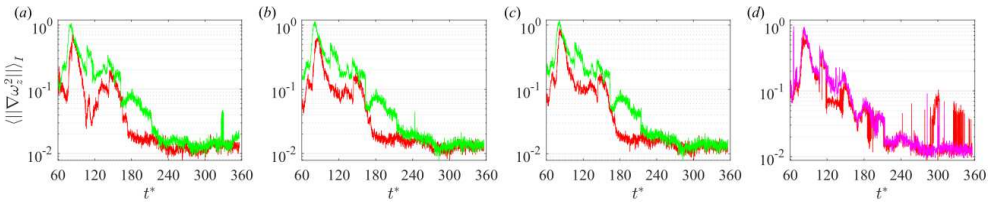


Fig. 16 Interface averaged enstrophy gradients as a function of time for the methods (a) M1, (b) M2, (c) M3 and (d) M4. The columns (i-ii) represent the two selected best cases from each method (marked by the symbols ▲ and ⋆ in figure 14).

Similarly, the enstrophy gradients averaged over the irrotational boundary (sampled on the x locations of the PIV grid) are further averaged over time and are shown in figure 14(b). Different colours are used for the different methods. For the methods M1, M2 and M3, the four threshold values selected are the ones for which the interfaces were shown in figures 4, 7 and 10 using the same colours. Note that the last thresholds (+) of each of the three methods capture the highest enstrophy gradients, however they miss a large portion of the total enstrophy indicating that the interfaces obtained for these cases were overly aggressive. In contrast, for the first thresholds (+) of each of the three methods, the interfaces overestimated the transverse extent of the wake. They thus captured nearly the entire enstrophy of the wake but failed to capture a significantly sharp enstrophy gradient. These results are in line with the visual observations from figures 4, 7 and 10. The intermediate threshold values (+ and +) do the best job as was seen previously and they capture $\geq 96\%$ of the total enstrophy (shown by the dashed line in figure 14(a)). We mark these two best working cases by ▲ and ⋆ in figure 14. Comparing the performance at these two intermediate threshold values we can say that the latter of the two (⋆) captures a significantly larger gradient at the expense of a small loss in total enstrophy. For instance, for M2, the average enstrophy gradient captured is nearly doubled for the latter threshold, while the loss in total enstrophy captured is only $\approx 2\%$. Therefore, we determine that the threshold values marked with a star yielded the best interfaces statistically. For simplicity, lets term these best cases as ⋆M# (where # denotes the method number, 1-3). The second best cases from each method are denoted as ▲M#. Note that among ⋆M1-3, ⋆M3 captured the highest total enstrophy as well as the highest enstrophy gradient, showing the efficacy of the I^2y transformation.

For the intensity-gradient based method, M4, the case without any image filtering or transformation clearly did not work, as shown in figure 12(a). Therefore, this case was excluded from figure 14. Although the next three cases seemed to work well from figure 12(b-d), when considering the entire time series, they capture a significantly lower proportion of the total enstrophy ($< 96\%$) as shown in figure 14. The best two cases are again marked with a ▲ and ⋆. The fact that these two cases considered filtered images and still failed to capture most of the total enstrophy statistically, highlights the difficulty associated with the gradient based technique.

To understand the underlying reason behind this sub-optimal performance of M4, we look at the time variation of the captured enstrophy fraction and enstrophy gradient for the two best cases from each method (⋆M# and ▲M#) in figures 15 and 16

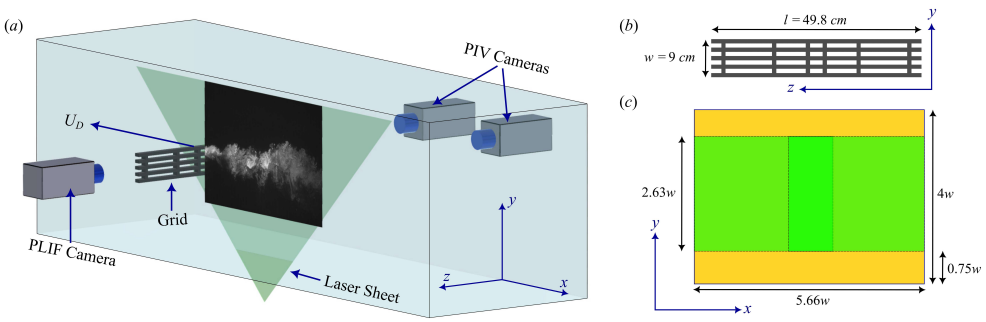


Fig. 17 (a) Experimental setup of the second experimental campaign involving a multiscale grid. Panel (b) shows the grid geometry. Panel (c) shows the PIV (green) and PLIF (yellow) field of view.

respectively. At several time instances, especially towards the end of the time series ($t^* > 240$), the gradient based method fails to capture any continuous contour at the chosen threshold, essentially capturing zero enstrophy. Additionally, at several time instances, it captures $< 50\%$ of the total enstrophy which is a result of a false detection or a detection of an internal contour. Supplementary movie 1 shows the time evolution of the interfaces for the best case ($\star$M#) of each of the four methods from $t^* = 240$. It can be readily seen that $\star$M4 is the most noisy and it suffers the most from the detection of internal contours. The intensity-based methods $\star$M1 and $\star$M2 although less noisy, still occasionally detect internal contours. As discussed previously, it is more likely to encounter the chosen intensity-gradient-based threshold within the turbulent core compared to the intensity-based threshold. Sometimes, these internal contours are longer than the true contour and are detected erroneously. Further constraints might therefore be required to choose the right interface from a set of interfaces instead of simply selecting the longest interface, which further obfuscates the implementation of the method. Among all the methods, the intensity-based method involving image transformation ($\star$M3), shows the least amount of noise and is deemed statistically the most appropriate for the current data set.

3 Decaying stream of grid turbulence

To assess the generalisability of the above conclusion that the I^2y technique (M3) shows a superior performance, the same set of interface detection techniques (methods 1-4) were applied to a different flow involving a decaying a stream of grid turbulence. For brevity, only the best cases from each of the methods are discussed.

Figure 17(a) shows a schematic of the experimental setup. A multiscale grid was moved upstream (along $-x$) at a velocity $U_D = 0.2$m/s. A small uniform background flow was run at 0.03m/s along the positive x direction to keep the large scale vortices shed by the grid within the FOV. Unlike campaign 1, the laser sheet and the field of view were aligned along the xy plane and the PIV and PLIF cameras were placed on the opposite sides of the flume as shown in figure 17(a). The grid had a width of w =9cm and length of l =49.8cm (see figure 17(b)). It consisted of 5 horizontal bars of length l and width 1cm. These bars had an uniform separation. The vertical bars

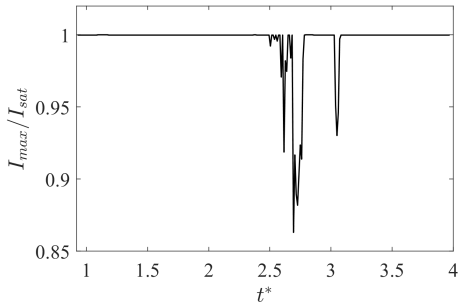


Fig. 18 Time history of maximum image intensity within the FOV.

of length = w had a non-uniform separation giving the grid a multiscale nature. The grid had an overall blockage of 60.91%. A total of three Phantom v641 cameras were used, two of them for PIV and one for PLIF, as shown in figure 17(a). The PIV and PLIF fields of view are shown in figure 17(c) in green and yellow respectively. The data was acquired in cinematographic mode at an acquisition frequency of 200 Hz. A total of 275 images (total time = 1.37 seconds) were used. Beyond this time, the dye concentration became too low in parts of the flow owing to the rapid mixing, hence the interface could not be obtained confidently with any of the methods. The scalar (Rhodamine 6g) was injected from the top bar of the grid as can be seen from figure 17(a). The scalar therefore only visualized the upper part of the wake. Consequently, we only focus on the upper TNTI.

The decaying turbulence behind the grid was significantly different from the cylinder wake in several ways. The grid turbulence was more three dimensional and multiscale in nature and had a larger Reynolds number (based on the width of the grid). Furthermore, for the grid, data was available for a shorter time span. The maximum light intensity (I_{max}) in the PLIF images normalized by the saturation intensity (I_{sat}) is shown in figure 18. Note that unlike for the cylinder (figure 2(b)), the PLIF images here remain locally saturated almost throughout the entire time span investigated.

For brevity, we do not discuss the process of identifying the thresholds for the different methods. We only discuss the interfaces obtained using the best threshold values for the four methods. These are shown in figure 19 at the first ($t^* = 0.93$) and the last ($t^* = 3.96$) time steps. Rows (a) - (c) correspond to the intensity based methods M1 - M3 as discussed previously. M4 corresponds to the gradient based method, where the filtered transformed images were used similarly to the case marked by magenta in figure 12 or figure 14. The images are filtered using the same NLM filter with the same degree of smoothness of 0.01. The images were then transformed to I^2y before computing the gradient. Note that the methods M1-M3 used the unfiltered images.

For this case, the four methods yielded similar looking interfaces and it was difficult to visually identify the best method. Nevertheless, certain method-specific drawbacks could be identified. M1 works well initially, but fails to capture a part of the turbulence towards the right edge of the FOV at the later time. For M2, the detected interfaces propagate into the non-turbulent background towards the left edge of the FOV. This

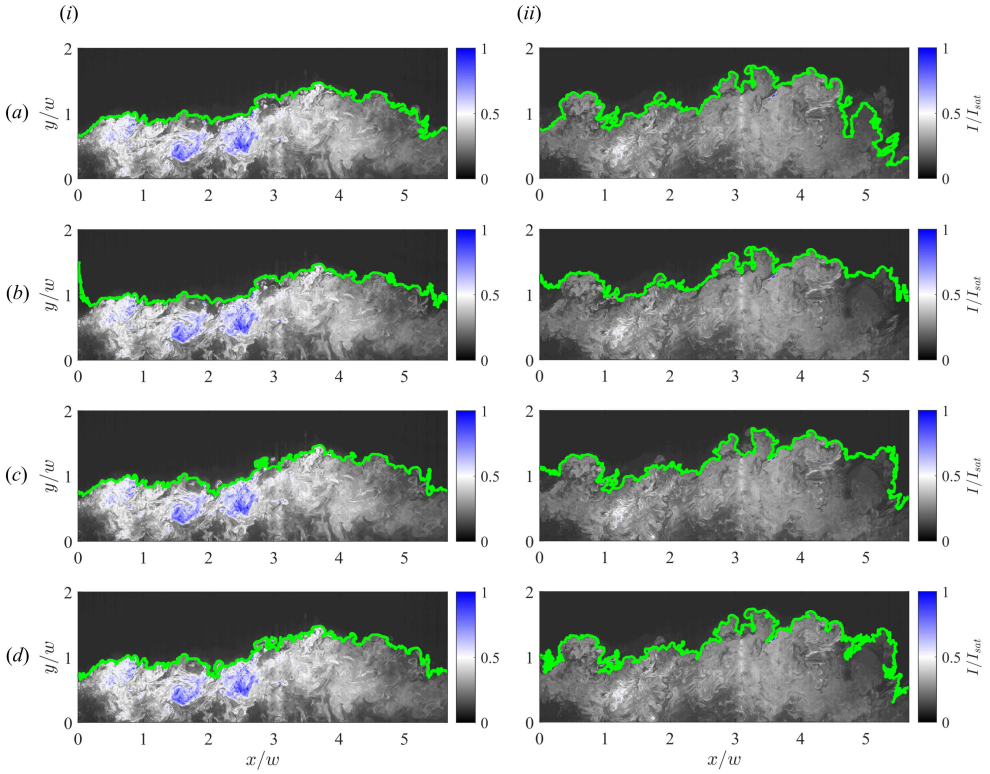


Fig. 19 Interfaces detected at (i) $t^* = 0.93$ and (ii) $t^* = 3.96$ using the methods (a) M1, (b) M2, (c) M3 and (d) M4.

is a drawback of the normalization process used here. At this location, the transverse width of the turbulent zone is significantly smaller (as a result of being closer to the grid), therefore, averaging the image intensity in y in this region yields a smaller value. Next, when the image is normalized with this smaller value, in the vicinity of $x/w = 0$, the region outside the wake gets assigned a relatively higher normalized intensity. Since, we are using the same cutoff throughout the time series, the interface propagates in the region outside the wake. This issue can be circumvented by setting up an iterative normalisation, where the image is averaged in y only up to the interface envelope instead of considering the whole transverse extent of the image. Therefore, we start with the interfaces shown in figure 19(b) and average the images only up to the interface envelope. These can next be used to normalise the raw images and repeat the interface identification process. We do not discuss this any further here but methods M2-M4 can easily be augmented with this iterative normalisation. For M3, this issue was less severe at initial times, but it eventually kicked in at later times. M4 seemed to work the best at these two instances. But note that M4 used filtered images while other methods did not. The full time series needs to be considered to identify the method that works the best statistically.

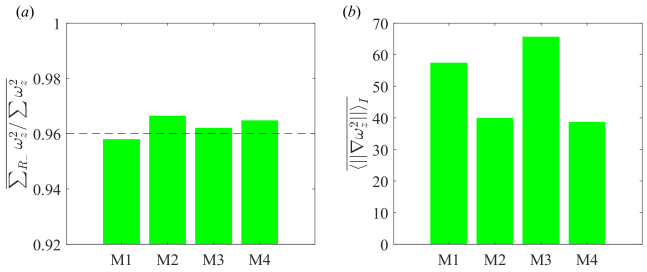


Fig. 20 Panel (a) shows the fraction of the total enstrophy in the FOV captured by the interface averaged in time for different methods. A horizontal dashed line is drawn at $\overline{\sum_{R_} \omega_z^2 / \sum \omega_z^2} = 0.96$. Panel (b) shows the time averaged magnitudes of enstrophy gradient averaged over the interface for the same methods and threshold values.

To better understand the relative performance of the four methods, we show the fraction of total enstrophy captured within the interfaces in figure 20(a) and the average enstrophy gradient over the interfaces in figure 20(b). Methods M2-M4 capture more than 96% of the total enstrophy and hence can be considered to be effective. Among these, the transformed intensity based method M3 captures the highest enstrophy gradient and hence can be considered the most effective statistically, similar to what was observed for the cylinder wake.

4 Conclusion

In this work we presented a robust methodology to identify turbulent/non-turbulent interfaces (TNTIs) in temporally-evolving turbulent flows. Two different flows were considered experimentally: 1) a temporally-evolving wake of a cylinder and 2) a decaying stream of grid turbulence. A high Schmidt number dye, rhodamine 6G, was used as a marker of the turbulence. Simultaneous Planar Laser Induced Fluorescence (PLIF) and Particle Image Velocimetry (PIV) experiments were performed to obtain the dye intensity (a surrogate of concentration) and the velocity fields respectively. The TNTIs were obtained using different methods based on PLIF image intensity (I) and its gradient-magnitude ($|\nabla I|$).

Previous PLIF-based studies on TNTIs mainly considered flows that are spatially developing, where the bulk concentration remained relatively constant over time (Westerweel et al. 2005; Mistry et al. 2016; Kankanwadi and Buxton 2020). For the present case, however, the PLIF signal decayed with time, hence requiring a time-dependent normalisation. Once the images are correctly normalised, a threshold is obtained by looking at the volume of turbulent fraction (f) similar to previous studies (Da Silva et al. 2014; Watanabe et al. 2015; Chen and Buxton 2024). For the image-intensity-based methods, the best-working thresholds could be objectively identified as a local extrema of the second derivative of f ($f^{''}$). Once the correct threshold was identified, the TNTI was identified as the longest continuous contour at the threshold value. Unlike the intensity-based methods, for the intensity-gradient-based method, the best working threshold did not correspond to a physically meaningful point in $f^{''}$ (either an extrema or inflection point(s)), making an objective identification of the

threshold difficult. Furthermore, it was shown that some degree of image filtering was necessary to implement the intensity-gradient-based method in order to reduce the elevated numerical noise associated with the computation of the spatial gradients. The intensity-based methods did not require any filtering.

A new intensity-based technique was proposed where the image intensity field was transformed using a combination of pixel-based intensity and the corresponding transverse (y) location of the form I^2y. Such a transformation promoted intensity in the vicinity of the actual interface and reduced the likelihood of detecting false internal contours. The efficiency of the different methods were compared using two metrics: (1) the average total enstrophy captured within the detected interfaces and (2) the enstophy gradient captured along the interfaces. The new I^2y based technique showed a superior performance for both the flows considered, consistently capturing a high total enstrophy and large enstrophy gradient. The intensity-gradient-based method was shown to work better when the gradient of I^2y was considered instead of I. The intensity-gradient-based method however suffered from frequent detection of internal contours at the chosen threshold value, statistically lowering its efficiency. The method would therefore require additional constraints to choose the right interface from a set of interfaces, adding to its complexity of implementation. For the intensity based techniques, simply choosing the longest contours at the identified threshold worked, making it a much simpler tool to implement. Nevertheless, simply choosing the longest continuous contour may not always guarantee the detection of the correct interface, especially if the span of the field of view considered is too small.

Author Contributions N.B. was involved in data collection, formal analysis, investigation, methodology and writing—original draft. J.C. was responsible for data collection, methodology, review and editing. O.R.H.B. took part in conceptualization, funding acquisition, methodology, supervision, review and editing.

Funding The authors gratefully acknowledge financial support from EPSRC fellowship grant no. EP/V006436/1 and ERC project funded through UKRI Horizons Europe guarantee grant no. EP/Z000149/1.

Acknowledgment N.B. acknowledges fruitful discussions with Dr. Lloyd Fung at Imperial College London.

Competing interests The authors declare no competing interests.

References

Antonia, R.A.: Conditional sampling in turbulence measurement. Annual review of fluid mechanics **13**, 131–156 (1981)

Baj, P., Bruce, P., Buxton, O.: On a plif quantification methodology in a nonlinear dye response regime. Experiments in Fluids **57**(6), 106 (2016)

Buxton, O.R., Chen, J.: The relative efficiencies of the entrainment of mass, momentum and kinetic energy from a turbulent background. Journal of Fluid Mechanics **977**, 2 (2023)

Buades, A., Coll, B., Morel, J.-M.: A non-local algorithm for image denoising. In: 2005 IEEE Computer Society Conference on Computer Vision and Pattern Recognition (CVPR'05), vol. 2, pp. 60–65 (2005). Ieee

Bisset, D.K., Hunt, J.C., Rogers, M.M.: The turbulent/non-turbulent interface bounding a far wake. Journal of Fluid Mechanics **451**, 383–410 (2002)

Chen, J., Buxton, O.R.: Spatial evolution of the turbulent/turbulent interface geometry in a cylinder wake. Journal of Fluid Mechanics **969**, 4 (2023)

Chen, J., Buxton, O.R.: Turbulent/turbulent entrainment in a planar wake. Journal of Fluid Mechanics **1000**, 26 (2024)

Chen, J., Buxton, O.R.H.: Non-local modulation of turbulent entrainment by coherent vortices in a translating-cylinder wake. Under review in the Journal of Fluid Mechanics (2026)

Corrsin, S., Kistler, A.L.: Free-stream boundaries of turbulent flows. Technical report (1955)

Da Silva, C.B., Hunt, J.C., Eames, I., Westerweel, J.: Interfacial layers between regions of different turbulence intensity. Annual review of fluid mechanics **46**(1), 567–590 (2014)

Huang, J., Burridge, H.C., Reeuwijk, M.: Local entrainment across a tnti and a tti in a turbulent forced fountain. Journal of Fluid Mechanics **977**, 13 (2023)

Kankanwadi, K.S., Buxton, O.R.: Turbulent entrainment into a cylinder wake from a turbulent background. Journal of Fluid Mechanics **905**, 35 (2020)

Kohan, K.F., Gaskin, S.: The effect of the geometric features of the turbulent/non-turbulent interface on the entrainment of a passive scalar into a jet. Physics of Fluids **32**(9) (2020)

Kohan, K.F., Gaskin, S.J.: On the scalar turbulent/turbulent interface of axisymmetric jets. Journal of Fluid Mechanics **950**, 32 (2022)

Mistry, D., Philip, J., Dawson, J.R., Marusic, I.: Entrainment at multi-scales across the turbulent/non-turbulent interface in an axisymmetric jet. Journal of Fluid Mechanics **802**, 690–725 (2016)

Prasad, R., Sreenivasan, K.: Scalar interfaces in digital images of turbulent flows. Experiments in fluids **7**(4), 259–264 (1989)

Silva, T.S., Silva, C.B.: The behaviour of the scalar gradient across the turbulent/non-turbulent interface in jets. Physics of Fluids **29**(8) (2017)

Taveira, R.R., Diogo, J.S., Lopes, D.C., Da Silva, C.B.: Lagrangian statistics across the turbulent-nonturbulent interface in a turbulent plane jet. Physical Review E—Statistical, Nonlinear, and Soft Matter Physics **88**(4), 043001 (2013)

Townsend, A.A.: The structure of turbulent shear flow (1956)

Thielicke, W., Stamhuis, E.J.: Pivlab–towards user-friendly, affordable and accurate digital particle image velocimetry in matlab. Journal of open research software **2**(1) (2014)

Watanabe, T., Silva, C.B., Nagata, K., Sakai, Y.: Geometrical aspects of turbulent/non-turbulent interfaces with and without mean shear. Physics of Fluids **29**(8) (2017)

Westerweel, J., Fukushima, C., Pedersen, J., Hunt, J.C.: Mechanics of the turbulent-nonturbulent interface of a jet. Physical review letters **95**(17), 174501 (2005)

Watanabe, T., Sakai, Y., Nagata, K., Ito, Y., Hayase, T.: Turbulent mixing of passive scalar near turbulent and non-turbulent interface in mixing layers. Physics of Fluids **27**(8) (2015)

Supplementary Files

This is a list of supplementary files associated with this preprint. Click to download.

- Supplementarymovie1.gif